WILEY | Hindawi

Research Article

Study on Hydrocarbon Accumulation Periods Based on Fluid Inclusions and Diagenetic Sequence of the Subsalt Carbonate Reservoirs in the Amu Darya Right Bank Block

Yunpeng Shan [ID]**, Hongjun Wang, Liangjie Zhang, Penghui Su** [ID]**, Muwei Cheng, and Zhenhua Bai**

PetroChina Research Institute of Petroleum Exploration and Development, Beijing 100083, China

Correspondence should be addressed to Yunpeng Shan; shan_yunpeng@petrochina.com.cn

In order to provide paleofluid evidence of hydrocarbon accumulation periods in the Amu Darya Right Bank Block, microexperiments and simulations related to the Middle-Upper Jurassic Callovian-Oxfordian carbonate reservoirs were performed. On the basis of petrographic observation, the diagenetic stages were divided by cathodoluminescence, and the entrapment stages of fluid inclusions were divided by laser Raman experiment and UV epifluorescence. The hydrocarbon generation (expulsion) curve and burial (thermal) history curve of source rocks were simulated by using real drilling data coupled with geochemical parameters of source rocks, such as total organic carbon (TOC) and vitrinite reflectance (R_o). The above results were integrated with microthermometry of fluid inclusions by inference the timing of hydrocarbon migration into the carbonate reservoirs. The horizon-flattening technique was used to process the measured seismic profile and restore the structural evolution profile. Four diagenetic periods and three hydrocarbon accumulation periods were identified. (i) For Syntaxial stage, the fluid captured by the overgrowing cement around particles is mainly seawater; (ii) for (Early) Mesogenetic burial stage, the calcite cements began to capture hydrocarbon fluids and show yellow fluorescence under UV illumination; (iii) for (Late) Mesogenetic burial stage, two sets of cleavage fissures developed in massive calcite cements, and oil inclusions with green fluorescence were entrapped in the crystal; (iv) for Telogenetic burial stage, blue fluorescent inclusions along with hydrocarbon gas inclusions developed in dully luminescent calcite veins. Based on the accurate division of hydrocarbon migration and charging stages, combined with the structural evolution history of the traps, the hydrocarbon accumulation model was established. Because two of the three sets of source rocks are of marine origin, resulting in the lack of vitrinite in the kerogen of those source rocks, there may be some deviation between the measured value of R_o and the real value. Some systematic errors may occur in the thermal history and hydrocarbon generation (expulsion) history of the two sets of source rocks. Due to the limitations of seismic horizon-flattening technique—such as the inability to accurately recover the inclined strata thickness and horizontal expansion of strata—the final shape of the evolution process of structural profile may also deviate from the real state in geological history. The accumulation model established in this study was based upon the fluid inclusion experiments, which can effectively characterize the forming process of large condensate gas reservoirs in the Amu Darya Right Bank Block and quantify the timing of hydrocarbon charging. However, the hydrocarbon migration and accumulation model does not take the oil-source correlation into account, but only the relationship between the mature state of source rocks and the timing of hydrocarbon charging into the reservoirs. Subsequent research needs to conduct refined oil-source correlation to reveal the relationship between gas, condensate, source rocks, and recently discovered crude oil and more strictly constrain and modify the accumulation model, so as to finally disclose the origin of the crude oil and oil reservoir forming process in the Amu Darya Right Bank Block, evaluate the future exploration potential, and point out the direction of various hydrocarbon resources (condensate gas and crude oil).

1. Introduction

The Amu Darya Right Bank Block (the block is denoted by ADRBB in the following text) project is the largest one for natural gas cooperation between China and Turkmenistan. According to the existing data and knowledge, the source rocks of the widely distributed condensate reservoirs in the ADRBB are primarily gas prone. In 2020, some reservoirs that mainly produce normal crude oil were discovered around large condensate gas reservoirs which produce condensate oil (this paper will be the first to report the discovery of crude oil in the ADRRB), indicating that we have not fully understood the regular pattern of hydrocarbon accumulation in the ADRBB. To ascertain the laws regarding the formation and distribution of hydrocarbon reservoirs in the ADRBB, there is an urgent need to restore and finely describe the formation and evolution process of reservoirs which should be regarded as individual units. We conduct various microscopic experiments such as cathodoluminescence of the Middle-Upper Jurassic Callovian-Oxfordian carbonate reservoirs in the ADRRB (the reservoir is represented by J_2k-J_3o in the following text) and the microthermometry and Raman spectrum of fluid inclusions of the J_2k-J_3o reservoirs. The experimental results are integrated with the burial (thermal) history to determine the reservoir charging period and stages. Then, based on the hydrocarbon generation (expulsion) history of source rocks and the structural evolution history of the strata, the forming process of hydrocarbon reservoirs is restored (Figure 1). The subsequent exploration and development of hydrocarbon reservoirs can be carried out on the basis of the formation process established in this paper.

Hydrocarbon charging and reservoir diagenesis are simultaneous geological processes in the petroleum system, and the constructive and destructive actions of diagenesis on the reservoir determine whether there is enough space to accommodate oil and gas. The various processes of porosity generation, preservation, and reduction "compete" with one another, and the present porosity and permeability characteristics represent the net result of all past processes [1]. Hence, to study the formation period of oil and gas reservoirs, it is necessary first to divide the diagenetic process of reservoirs in a certain area in detail. Constructive diagenesis includes dissolution, dolomitization [2], and tectonic faulting. Destructive diagenesis includes compaction, cementation, stylolitization, and recrystallization. Other diagenesis, such as hydrocarbon generation overpressure in shale, also belongs to positive diagenesis. The generated gas will make the laminated shales open more in the bed-normal direction, which favors incipient vein opening between laminae, even in the absence of deviatoric stress [3]. Veins filled with brittle minerals, such as quartz or calcite veins, are more conducive to the generation of fractured media, which is highly significant for the production of shale gas [4] and the immiscible two-phase flow (in oil zone with a gas cap) displacement [5]. Bacterial sulfate reduction (BSR) and thermochemical sulphate reduction (TSR) have the nature of a double-edged sword for reservoir reconstruction. On the one hand, these two reactions will dissolve sulfate, produce acid gas (H_2S,

CO_2), and form secondary pores. On the other hand, solid bitumen may form as a by-product of both BSR and TSR to block pores. Therefore, for blocks with these two redox reactions, the effect of BSR/TSR on reservoir reconstruction needs to be comprehensively evaluated [6]. Cathodoluminescence is a powerful means to determine diagenetic minerals and formation stages, because different minerals precipitated in the same period, or the same mineral precipitated in different periods, show different cathodoluminescence properties [7]. The microthermometry and Raman spectrum of secondary fluid inclusions can provide direct data for the timing of the entrapment, and the structural recovery from real data of traps can show the formation process of hydrocarbon reservoirs specifically and help delimit the migration pathways of oil and gas [8].

2. Geology Overview

The Amu Darya Basin, located in eastern Turkmenistan and southwestern Uzbekistan, is a large gas-rich foreland basin in Central Asia. It covers an area of $42.70 \times 10^4 \, \text{km}^2$ and has proven recoverable oil reserves of $1.7 \times 10^8 \, \text{t}$ and proven recoverable natural gas reserves of $22 \times 10^{12} \, \text{m}^3$ [9]. The Amu Darya Basin has been in the northern margin of the Tethyan tectonic domain since the Late Paleozoic. The basin has mainly experienced the Late Paleozoic-Early Mesozoic basement development period, the Permian-Triassic rifting period, the Jurassic-Paleogene Eocene postrifting depression period, and the Neogene Miocene-Quaternary foreland basin period [10]. In terms of the current basement undulation and sedimentary caprock structure state, the Amu Darya Basin is divided into structural units such as Kopet-Dag piedmont depression, Chardzhou terrace, Carlabekaul depression, Bieshikent depression, Murgab depression, and central Karakum uplift. The ADRBB is located in the northeast of Amu Darya basin, covers an area of $1.43 \times 10^4 \, \text{km}^2$ and traverses 3 secondary structural units such as Chardzhou terrace, Bieshikent depression, and southwest Gissar thrust belt [11, 12]. The ADRBB can be further divided into 6 structural units such as Chardzhou uplift, Kennedykiddskurt uplift, Sandykly uplift, Carlabekaul depression, Bieshikent depression, and southwest Gissar piedmont thrust belt (Figure 2(a)).

The ADRBB has experienced the evolution process of continental-marine-lagoon facies. After being uplifted in the Late Triassic, the ADRBB reentered a subsidence stage in the Early-Middle Jurassic. The depositional environment of the ADRBB gradually changed from delta to marine facies. The Middle-Lower Jurassic coal-bearing mudstones with a basin scale deposited in this period in the Amu Darya Basin are the most important set of source rocks in the basin [13]. The ADRRB experienced a large-scale transgression in the Callovian period of the Middle-Late Jurassic, and a Callovian gentle slope carbonate platform developed on the basis of the formed accommodation space in this period. During the Oxfordian period of the Middle-Late Jurassic, the ADRRB suffered another large-scale transgression. The platform was generally submerged, and it retreated, and a rimmed shelf-type carbonate platform formed. The two
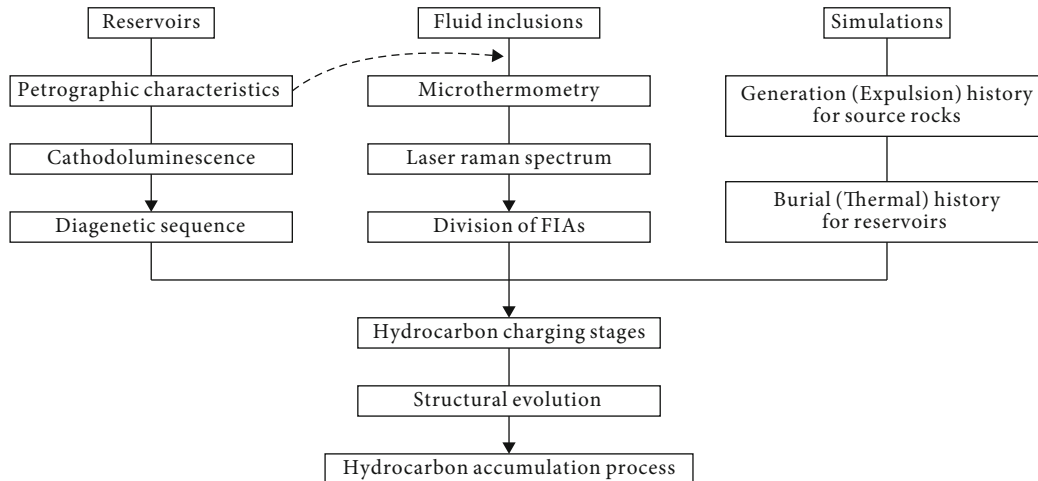
FIGURE 1: Specific research ideas on the hydrocarbon accumulation process of the ADRRB. The dashed line in the figure indicates that petrographic observation is also required when dividing FIAs. Fluid inclusion assemblage (FIA) is defined as all inclusions along the same growth zone in a single crystal or all inclusions along a single healed fracture, usually present in clusters or in a consistent extension direction [7].

stages of platform facies deposition in the ADRBB have resulted in the development of superimposed intraplatform mound-beach carbonate reservoirs in the western section and the development of longitudinally aggradational gentle-slope reef-beach carbonate reservoirs in the mid-eastern section [14, 15]. The deposited carbonate reservoirs are mostly argillaceous limestones with high organic matter content and are a set of main source rocks in the Jurassic in the ADRBB. As the seawater grew deeper, a deep mudstone layer (Gap layer) with high gamma-ray value developed in the mideastern section of the ADRBB at the end of the Oxfordian period. The thickness of the Gap layer is mostly less than 20 m; it is a set of secondary source rocks of the Jurassic in the ADRBB. That is, working upwards, there are three sets of source rocks in ADRBB: coal-bearing mudstone, argillaceous limestone, and the Gap layer. At the same time of the development of the Gap layer, the ADRBB began to retreat on a large scale, and the reefs disappeared in most regions. In the Late Jurassic Kimmeridgian period, the ADRBB began to enter the gypsum deposition stage, and the carbonate platform gradually degenerated into a gypsum platform. From the Late Jurassic Kimmeridgian period to the Tithonian period, the ADRBB experienced multiple periods of transgression and regression, where thick "three anhydrite units and two salt units" layers were deposited [16]. Three sets of source rocks and J_2k-J_3o carbonate reservoirs, together with the ultrathick anhydrite-salt layer, constitute a complete set of source-reservoir-caprock assemblages of continuous sedimentation from bottom to top. The excellent hydrocarbon accumulation assemblage provides the material basis for the formation of large-scale subsalt hydrocarbon reservoirs in the ADRBB [17, 18] (Figure 2(b)).

After ten years of exploration and development of the ADRBB, more than 40 hydrocarbon reservoirs have been discovered, which are distributed in the west, middle, and east sections and are mainly natural gas reservoirs. The reservoirs are substantially structural traps controlled by anticlines and faults, followed by structural-lithological traps (Figure 2(c)). The western reservoirs are pore-vug type. These are multilayer large-scale intraplatform beach bodies, with secondary pores and residual primary pores as the dominating reservoir space and auxiliary solution cavities. The middle reservoirs are fracture-pore type. These are extensive gentle-slope reef-beach groups, and the reservoir space is dominated by secondary dissolution vugs and fractures. The east reservoirs are fracture-vug type. These are massive fracture-vug carbonate reservoirs related to thrust structures, and the reservoir space is fractures; vugs dissolved along fractures and irregular solution holes. Fractures and faults are pervasive in the subsalt reservoirs and play a significant role in improving the migration pathways and reservoir space. The temperature of the primary pay formation is 100°C-140°C; the salinity of NaCl of formation water is 3-7% [19], and the pressure factor ranges from 0.8 to 2.0; the composition of the well fluids is dominated by CH_4, and their average volume fraction is below 95%, showing normal/high pressure wet gas reservoirs with a normal temperature system.

3. Materials and Methods

The core samples were collected from the major gas-bearing horizons of J_2k-J_3o in the 7 high yield wells. Wells AWS-5 and AWM-2 are located in the west section of ADRRB, while wells AMP-1, AMO-2, and AMB-1 are located in the middle section. Wells AEA-1 and AEA-2 are located in the east section (Figure 2(a)). Core samples were made into standard double-sided polished slices for inclusion observation.

Petrographic observation was performed using Zeiss AxioCamERc5s microscopes. The vacuum of the cathodoluminescence instrument is 0.3 Pa. The voltage and current of the electron beam are 7.5 kV and 0.63~0.76 mA, respectively. The microthermometry data were obtained using Linkam
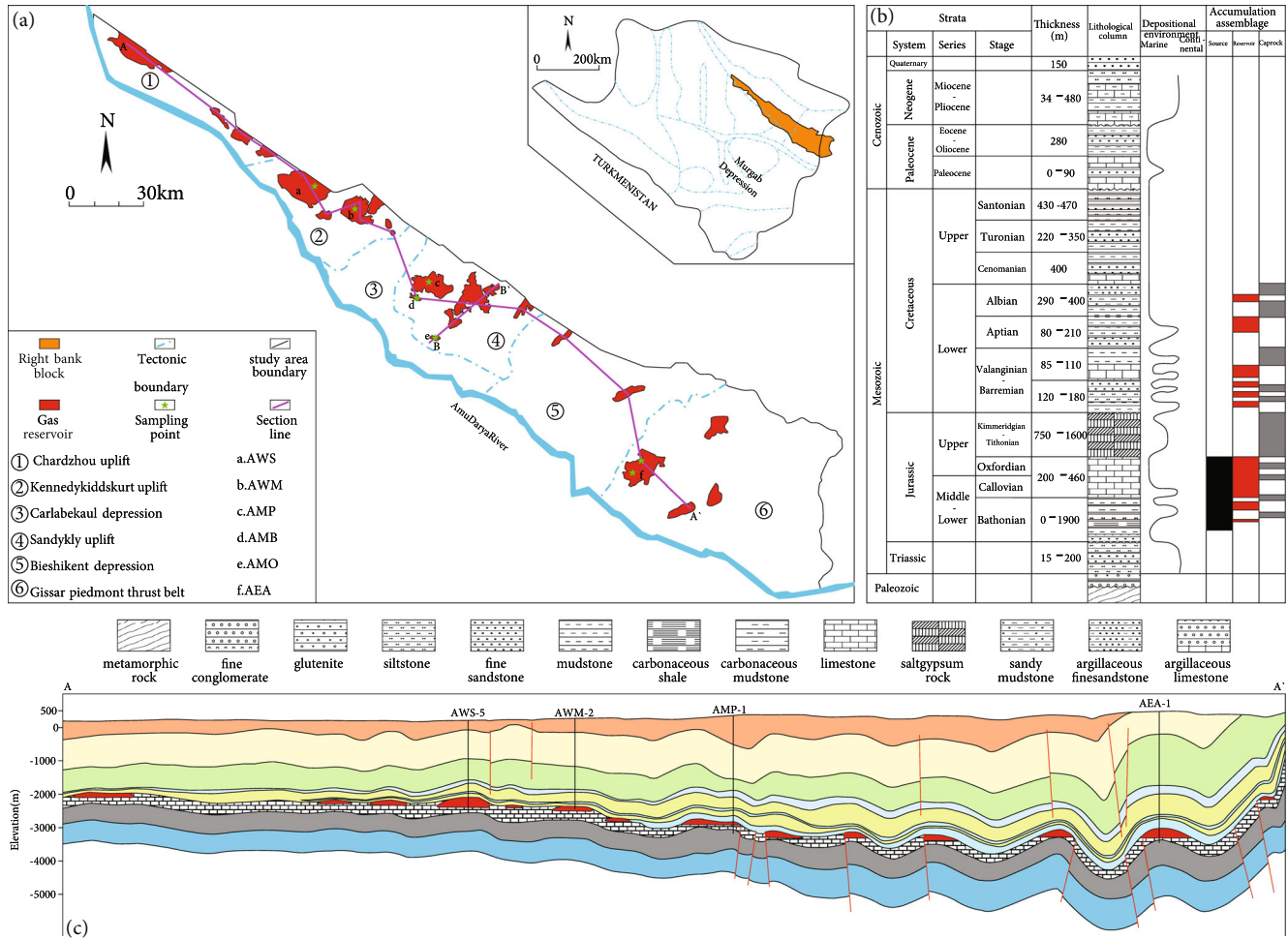
(a)

Right bank block
Gas reservoir
① Chardzhou uplift
② Kennedykiddskurt uplift
③ Carlabekaul depression
④ Sandykly uplift
⑤ Bieshikent depression
⑥ Gissar piedmont thrust belt

Tectonic boundary
Sampling point
Section line

study area boundary

a.AWS
b.AWM
c.AMP
d.AMB
e.AMO
f.AEA

TURKMENISTAN
Murgab Depression
AmuDaryaRiver

(b)

Strata			Thickness (m)	Lithological column	Depositional environment Marine / Continental	Accumulation assemblage Source / Reservoir / Caprock
System	Series	Stage				
Cenozoic Quaternary			150			
	Neogene	Miocene Pliocene	34 ~480			
	Paleocene	Eocene Oliocene	280			
		Paleocene	0 ~90			
Mesozoic Cretaceous	Upper	Santonian	430 -470			
		Turonian	220 ~350			
		Cenomanian	400			
	Lower	Albian	290 ~400			
		Aptian	80 ~210			
		Valanginian	85 ~110			
		Barremian	120 ~180			
Jurassic	Upper	Kimmeridgian Tithonian	750 ~1600			
	Middle - Lower	Oxfordian	200 ~460			
		Callovian				
		Bathonian	0 ~1900			
Triassic			15 ~200			
Paleozoic						

metamorphic rock | fine conglomerate | glutenite | siltstone | fine sandstone | mudstone | carbonaceous shale | carbonaceous mudstone | limestone | saltgypsum rock | sandy mudstone | argillaceous finesandstone | argillaceous limestone

(c)

A — AWS-5 — AWM-2 — AMP-1 — AEA-1 — A'
Elevation(m): 500, 0, -1000, -2000, -3000, -4000, -5000

Figure 2: Structural units, the location of sampling points, composite stratigraphic columnar section, and gas reservoir profile in the Amu Darya Right Bank Block.

THMS-600 cooling/heating stage, with the temperature measurement range of -196~600°C, and the measurement error of ±0.1°C. Raman spectra were collected by using a JY/Horiba LabRam HR800 Raman system equipped with a frequency doubled Nd: YAG laser (532.06 nm), whose output laser power is 45 mW and a 50× longworking-distance Olympus objective with a 0.5 numerical aperture. Spectra were collected in the range of ~100–4000 cm^{-1}. The acquisition time was approximately 1 s, with two accumulations for each spectrum to maintain a high signal-to-noise ratio. Before Raman testing, the instrument was calibrated with monocrystalline silicon whose Raman shift should be 520.70 cm^{-1}.

In order to gain a deeper understanding of accumulation period of the ADRRB, we used the PetroMod 2016 software to recover the hydrocarbon generation and expulsion history of source rocks. At the same time, the stratigraphic burial and thermal history of source rocks and structural evolution history were restored. The concepts and rules of restoration are based on the methods discussed by Hantschel and Kauerauf [20]. The maturity data of source rocks are obtained from the measured vitrinite reflectance (R_o). The present strata thickness is obtained from drilling and logging data. The total organic carbon (TOC) and Hydrogen Index (HI) data are obtained from pyrolysis testing. The thermal history curves are restored according to the geothermal gradient of 4.0°C/100 m in the uplift area and 2.5°C/100 m in the depression area and the surface temperature of 20°C, and the thermal history curves are constrained and corrected by R_o.

4. Results and Discussion

4.1. Cathodoluminescence and Diagenetic Sequence. The order of luminescent color of J_2k-J_3o is nonluminescent, brightly red, brightly orange, and dully luminescent. In general, incorporation of Mn^{2+} into the calcite lattice stimulates luminescence, and incorporation of Fe^{2+} reduces or quenches luminescence. The cathodoluminescence properties of carbonate particles with different structures and compositions are obviously different. The pictures in Figure 3 are shown in pairs. Each pair of pictures is taken in plane-polarized light and cathodoluminescence with the same area.

Micritic calcite and intraclast show dully reddish luminescent while bioclasts are nonluminescent (Figures 3(a) and 3(b)). Fluid inclusions do not develop in micritic calcite but
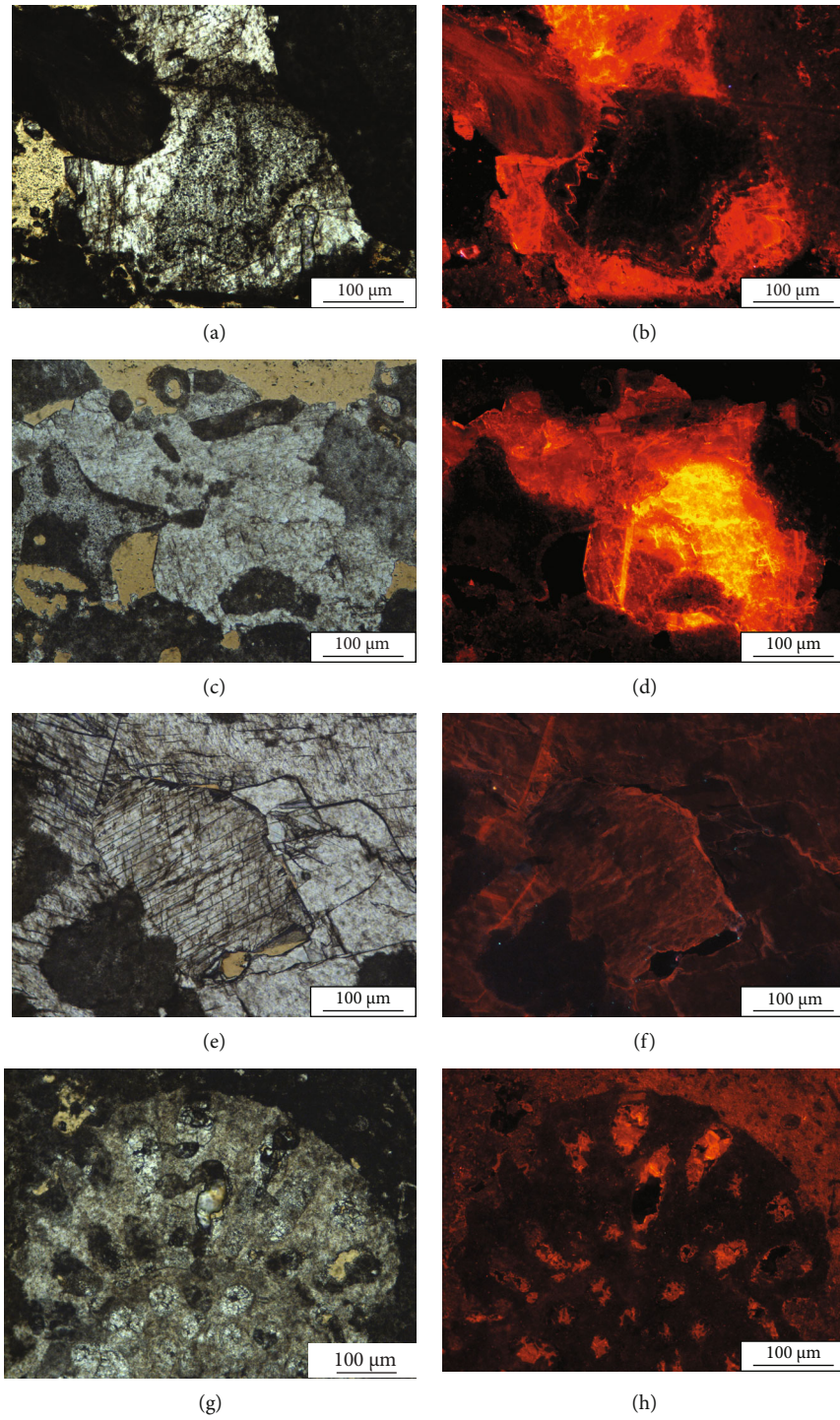
(a)

(b)

(c)

(d)

(e)

(f)

(g)

(h)
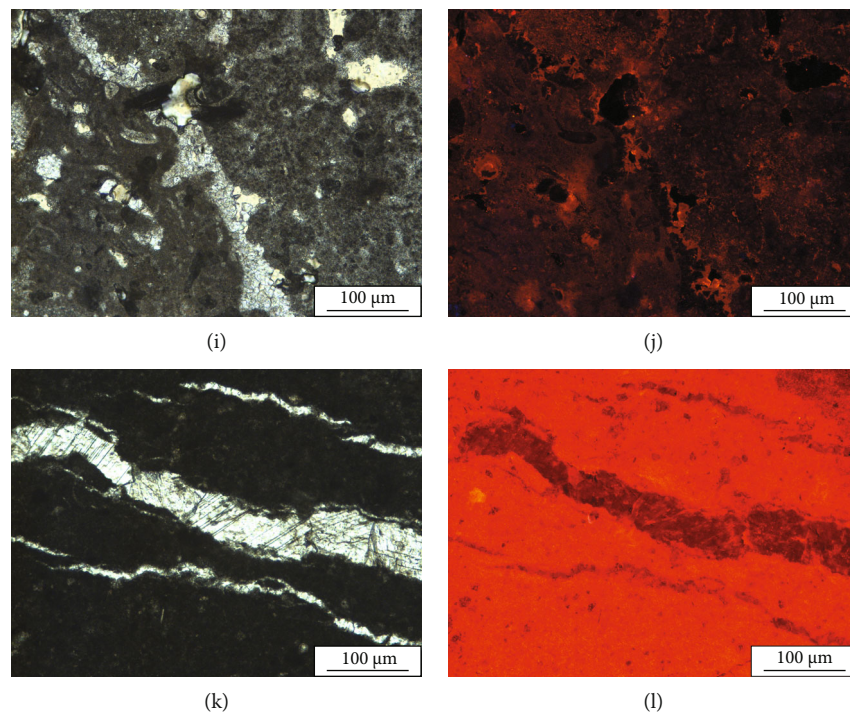
Figure 3: Continued.

(i)

(j)

(k)

(l)

FIGURE 3: Cathodoluminescence characteristics of the J_2k-J_3o reservoirs in the ADRRB.

may develop in intraclast and bioclast. However, the fluid inclusions developed in these two kinds of particles are primary inclusions, not secondary inclusions trapped during burial diagenesis. So we do not focus on these three carbonates.

According to the luminescent characteristics and relative positions, the sparry calcite cements that can develop secondary fluid inclusions can be divided into four stages.

(i) *Syntaxial Cements*. It is difficult to identify syntaxial overgrowth cement in plane-polarized light. Syntaxial overgrowth cements keep in optical continuity with their substrate under the condition of cathodoluminescence [21]; that is, they are nonluminescent. The syntaxial cements are serrated (Figures 3(a) and 3(b))

(ii) *(Early) Mesogenetic Burial Cements*. Generally, they grow around particles or micritic calcite matrix (Figures 3(c) and 3(d)). However, they may also grow around syntaxial cements (Figures 3(a) and 3(b)). The crystal shape is mostly massive ($>100 \mu m$) but also some granular ($<10 \mu m$). They are brightly red luminescent

(iii) *(Late) Mesogenetic Burial Cements*. In general, they fill pores that are not filled with (i) and (ii) cements. They will grow around the micrite calcite matrix or be surrounded by the (ii) cement (Figures 3(c) and 3(d)), showing massive structure. Cleavage fissures of some massive calcite are well developed (Figures 3(e) and 3(f)). The (iii) cements can also fill in the body chamber of the bioclast in an equant granular form (Figures 3(g) and 3(h)). The (iii)

cements are brightly orange luminescent. The equant granular calcites are accompanied by two generations of calcite cement (Figures 3(i) and 3(j)). The earlier generation is bladed and nonluminescent. The bladed cements are probably an early syntaxial diagenetic product that altered or formed overgrowths on, marine cement precursors. The second generation cements are equant granular calcites with orange cathodoluminescence

(iv) *Telogenetic Burial Cements*. There are calcite veins in the rock samples, and the calcite particles are brighter than other three-stage cements in plane-polarized light. At least one group of cleavage fissures can be clearly identified. They are dully luminescent under cathodoluminescence (Figures 3(k) and 3(l))

In short, the cement in reservoir pores is calcite which can be determined by cathodoluminescence and petrographic analysis. We have defined four diagenetic periods. The diagenetic periods are (i) Syntaxial stage, (ii) (Early) Mesogenetic burial stage, (iii) (Late) Mesogenetic burial stage, and (iv) Telogenetic burial stage. Figure 4 is a comprehensive sketch of Figure 3 showing all diagenetic stages, in which fluid inclusion assemblages developed in sparry calcite cements are also shown. The stages and corresponding characteristics of fluid inclusions developed at different locations will be discussed in Section 4.2.

4.2. Petrographic Characteristics and Microthermometry of Fluid Inclusion. Considering the phase state at room temperature and fluorescence characteristics of fluid inclusions,
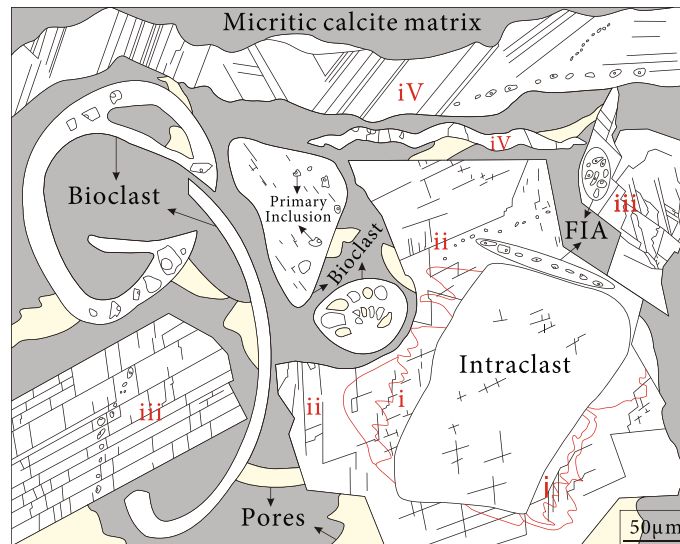
FIGURE 4: Schematic representation of different diagenetic sequences and fluid inclusion stages. The serrated red lines show the boundary between (i) and (ii) calcite cements. The two phases cannot be distinguished in plane-polarized light. With cathodoluminescence illumination, the (i) overgrowth cements maintain the same nonluminescent properties as the intraclast, while the (ii) cements are brightly red luminescent, as shown in Figures 3(a) and 3(b). (i) Syntaxial calcite cement; (ii) (Early) Mesogenetic calcite cement; (iii) (Late) Mesogenetic calcite cement; (iv) (Late) Mesogenetic calcite veins.

they are classified into four types: (i) gas inclusions, (ii) aqueous inclusions, (iii) two-phase aqueous inclusions, and (iv) two-phase hydrocarbon inclusions.

(i) *Gas Inclusions*. The gas inclusions have mainly developed in calcite veins. They also have a relatively dark appearance owing to their high relief, which commonly discriminates them from aqueous liquid inclusions in plane-polarized light. They have no fluorescence under ultraviolet epi-fluorescence. The size of the gas inclusion is small, and their length and width are about 3 μm (Figures 5(a) and 5(b))

(ii) *Aqueous Inclusions*. The aqueous inclusions have developed in the four stages of sparry cements. They are colorless and essentially transparent in plane-polarized light and are nonfluorescent under ultraviolet epi-fluorescence. They are mainly distributed in the healing fractures of calcite and are oriented. Some aqueous inclusions are also distributed in groups, clusters, or disorder. The aqueous inclusions show a single liquid phase, and their size is similar to that of gas inclusions (Figures 5(c) and 5(f))

(iii) *Two-Phase Aqueous Inclusions*. The environment for the formation of two-phase aqueous inclusions is essentially the same as that of aqueous inclusions. The optical characteristics of two-phase aqueous inclusions are the same as those of aqueous inclusions. However, when some inclusions are formed, some gases are dissolved in the fluid (note that the fluid in this period is homogeneous), and then, the gases resolve to form a vapor bubble with the change of P-T condition. Therefore, in most cases, two-phase aqueous inclusions coexist with aqueous

inclusions (Figures 5(c) and 5(f)). When heated during microthermometry, these inclusions typically homogenize to the liquid phase

(iv) *Two-Phase Hydrocarbon Inclusions*. The two-phase hydrocarbon inclusions formed during the period of hydrocarbon charging. They are blackish with a small vapor bubble. The bubble is more likely to be in pseudo-brownish motion than in aqueous inclusions with the same volume ratio of gas to liquid. When the composition and maturity of trapped hydrocarbon are different in each period, the fluorescence color of the corresponding inclusions will be different [22–24]. There are three fluorescent colors of two-phase hydrocarbon inclusions in J_2k-J_3o—yellow, green, and blue. The yellow fluorescent inclusions mainly developed in the (Early) Mesogenetic burial cements (Figures 5(g) and 5(h)). The green fluorescent inclusions mainly developed in the (Late) Mesogenetic burial cements (Figures 5(i) and 5(j)). The blue fluorescent inclusions mainly developed in the Telogenetic burial cements (Figures 5(k) and 5(l)). The three fluorescence colors may indicate that ADRRB experienced at least three stages of oil and gas charging. Additionally, inclusions showing green and blue fluorescence are evidently less abundant than those showing yellow fluorescence, while the hydrocarbon fluid charging intensity is the dominating factor affecting inclusions abundance [25, 26], indicating that the hydrocarbon charging scale with yellow fluorescent inclusions formed is the largest

The homogenization temperature (T_h) of hydrocarbon inclusions is generally hard to detect due to the thermal instability of the organic matter and T_h differences of each
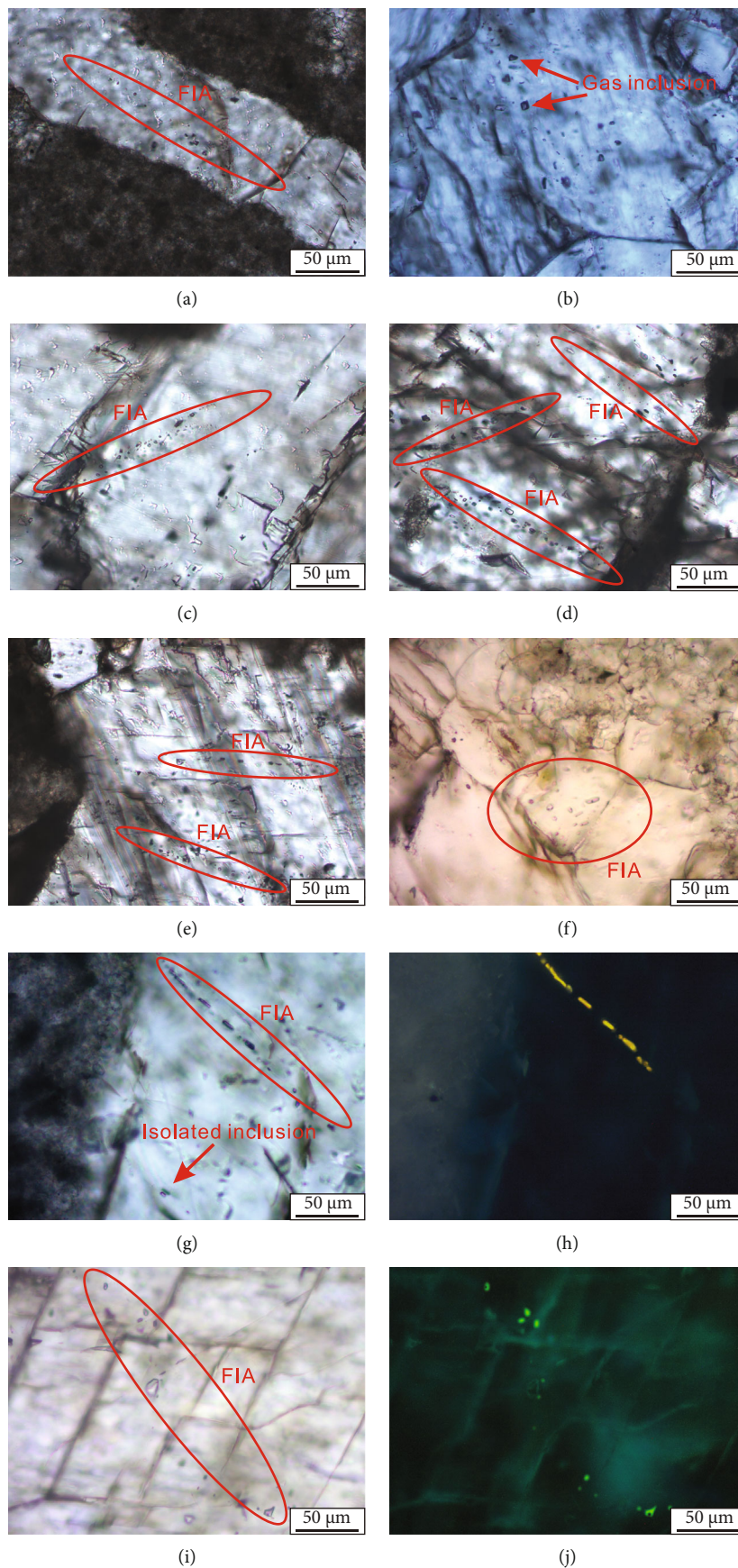
(a)

(b)

(c)

(d)

(e)

(f)

(g)
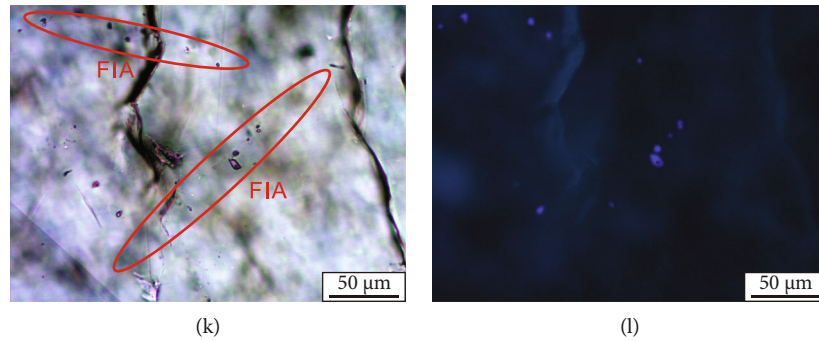

(h)

(i)

(j)

FIGURE 5: Continued.

(k)

(l)

FIGURE 5: Microscopic features of fluid inclusions in the J$_2$k-J$_3$o reservoirs in the ADRRB. (a) Well AMO-2, FIA in calcite veins; (b) Well AEA-1, gas inclusions coexisting with two-phase aqueous inclusions in calcite veins; (c, d) Well AMO-2, FIA in (Early) Mesogenetic burial calcite cements; (e) Well AMO-2, FIA in (Late) Mesogenetic burial calcite cements. The extension direction of FIA cuts the cleavage fissures of the calcite; (f) Well AEA-2, FIA in cluster distribution. The aqueous inclusions have a constant gas-liquid ratio and T_h; (g, h) Well AMO-2, yellow fluorescent hydrocarbon inclusions in the healing fracture of (Early) Mesogenetic burial calcite cements; (i, j) Well AMO-2, green fluorescent hydrocarbon inclusions in the healing fracture of (Late) Mesogenetic burial calcite cements. The extension direction of FIA cuts the cleavage fissures of the calcite; (k, l) Well AMO-2, blue fluorescent hydrocarbon inclusions in the calcite veins.

phase present within such inclusions. If aqueous and hydrocarbon inclusions coexist and their capture within a host mineral can be referred to the same P-T conditions, the T_h of aqueous inclusions could give information also about hydrocarbon ones. For the selection of fluid inclusions in the process of microthermometry, the aqueous inclusions which belong to the same fluid inclusion assemblage (FIA) with hydrocarbon inclusions are selected [7, 27]. The best development location of FIA is in the healing fractures of calcite. FIA can also be recognized in the growth zones of calcite with different cathodoluminescence colors. In the same FIA, the T_h of all fluid inclusions is relatively consistent, and the difference remains in the range of 10-15°C. If the difference value is beyond that range, it means heterogeneous trapping, necking down, or stretching of fluid inclusions, so this set of data is discarded. Generally speaking, clustered or grouped distribution of fluid inclusions is not a good indicator of FIA, but if the T_h and vapor-liquid ratio of fluid inclusions are relatively consistent, the cluster or group of fluid inclusions can still be considered as a FIA.

When the formation is not saturated with gas, the T_h of inclusions is often lower than the actual trapped temperature and needs to be corrected. When the formation is saturated with gas, the T_h of inclusions can represent the trapped temperature. Since the Amu Darya Basin is rich in natural gas, it is assumed that the T_h is tested when the formation is saturated with gas.

Using histograms enables effective visual display of the data on the thermal history of multiple phases. The T_h histogram of fluid inclusions was plotted (Figures 6(a) and 6(b)) in accordance with the method of FIA and microthermometry data (Table 1). Figure 6(a) is the T_h histogram of all aqueous fluid inclusions. Figure 6(b) is the T_h histogram of aqueous inclusions which belong to the same FIA with hydrocarbon inclusions showing three fluorescent colors in Well AMO-2. It can be seen from Figure 6(a) that the prevailing T_h of the fluid inclusions in the ADRRB is 90~140°C, with continuous distribution characteristics, indicating that on the whole the basin is in a continuous charging state. The main peak temperature is 100~110°C, reflecting the overall large-scale hydrocarbon charging of one stage. The T_h of the inclusions in the samples from Well AMO-2 is 90~160°C, and the two peak temperatures are 100~110°C and 130~140°C (Figure 6(b)). The T_h data of 100-110°C correspond to yellow fluorescent hydrocarbon inclusions, while T_h data of 130-140°C correspond to green and blue fluorescent hydrocarbon inclusions. The T_h of some fluid inclusions reaches 150-160°C, which exceeds the highest formation temperature in geological history (the strata have not experienced large-scale uplift, so the current formation temperature is the highest temperature in geological history). The reason may be that the deep hydrothermal fluids were trapped. Or when the fluid inclusions were formed, the fluids were not in a homogeneous phase state but immiscibly trapped, so that the T_h measured is far higher than the formation temperature when the fluid inclusions were trapped [28, 29].

The salinity of NaCl is determined by Bodnar's formula [30] using freezing point depression data (Figures 6(c) and 6(d)). It can be seen from Figure 6(c) that the T_h and the salinity of these secondary inclusions show a certain degree of positive correlation. The T_h of fluid inclusions in AMO-2 well in the range of 130-140°C can be divided into two periods by using salinity data (Figure 6(d)). The salinity of the fluid inclusions of the three stages is 2.90~8.41%, 8.14~12.73%, and 4.49~9.86%.

4.3. Characteristics of Laser Raman Spectrum. Laser Raman spectroscopy can be used for qualitative identification of the components of minerals and fluid inclusions to provide evidence for petrographic analysis. The fluorescence intensity of liquid hydrocarbon is several orders of magnitude higher than that of Raman spectrum intensity. So the laser Raman experiments can only be carried out in gas inclusions and (two-phase) aqueous fluid inclusions.
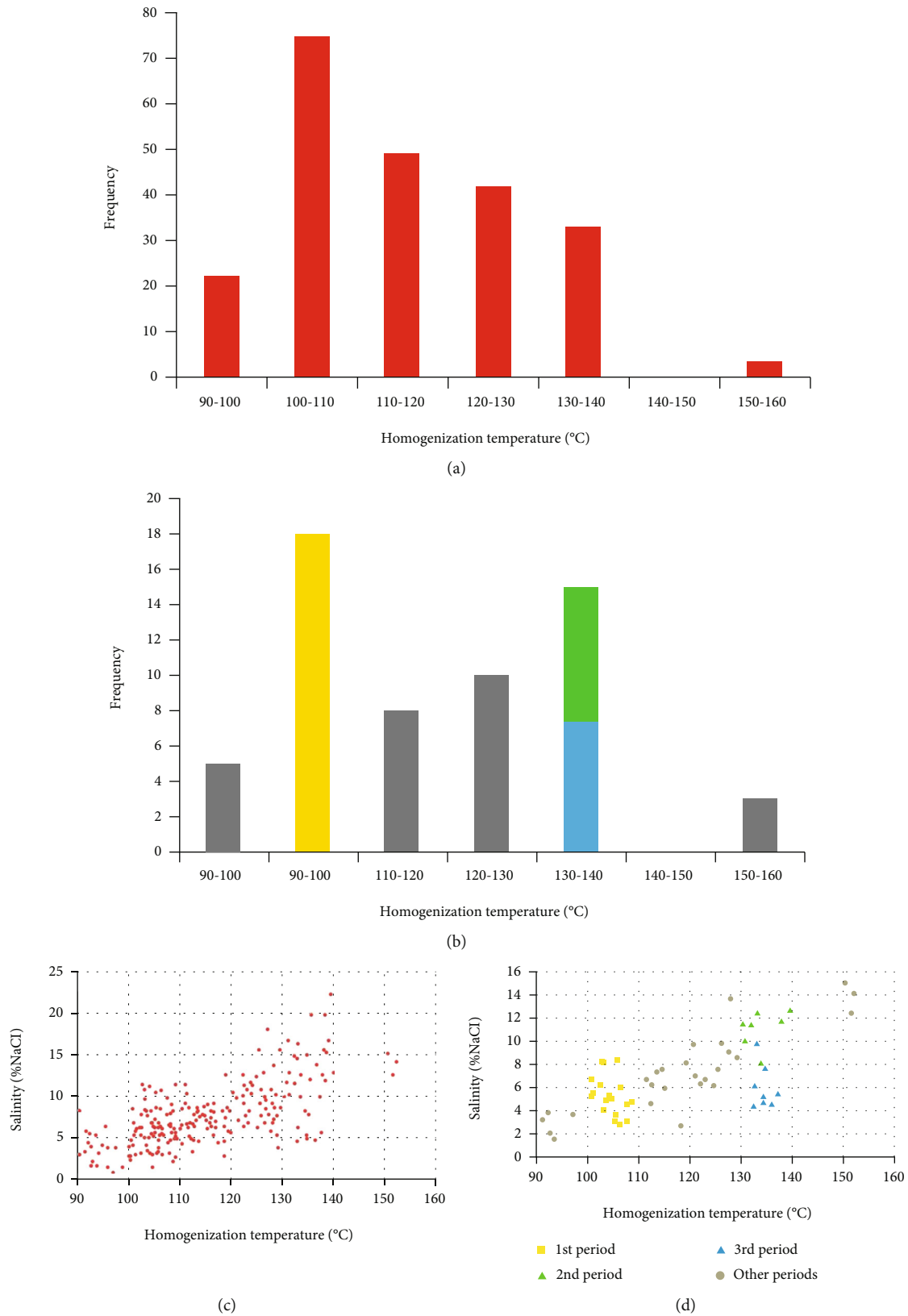
(a)

(b)

(c)

(d)

FIGURE 6: Microthermometry diagram of fluid inclusions in the J_2k-J_3o reservoirs in the ADRRB: (a) T_h histograms of all aqueous fluid inclusions in this study; (b) T_h histograms of aqueous fluid inclusions in AMO-2; (c) T_h-salinity plot of all aqueous fluid inclusions; (d) T_h-salinity plot of aqueous fluid inclusions in AMO-2.

TABLE 1: Microthermometry data of fluid inclusions in the in the J_2k-J_3o reservoirs in the ADRRB.

Well no.	Depth (m)	FIA type	Homogenization temperature (°C)	Freezing point (°C)	Salinity (% NaCl)
AWS-5	2462.05	Healing fracture	102.4 ~ 128.1	-7.7 ~ -14.2	11.34~17.96
AWM-2	2668.23	Cluster	100.5 ~ 127.9	-5.4 ~ -19.7	8.41~22.17
AMB-1	3147.17	Healing fracture	101.3 ~ 138.8	-3.7 ~ -8.8	6.01~12.62
AMO-2	3828.92	Healing fracture	92.4 ~ 152.3	-0.9 ~ -11.1	1.57~15.07
AMP-1	3180.03	Cluster	90.1 ~ 132.7	-5.2 ~ -12.7	8.14~16.62
AEA-1	3609.42	Healing fracture	95.6 ~ 129.1	-0.8 ~ -16.3	1.40~19.69
AEA-2	3300.8	Cluster	91.8 ~ 126.2	-2.6 ~ -11.5	4.33~15.47

The four stages of sparry cements classified by petrography were tested separately. The results show that the Raman shift of the highest peak of stage (i) (Figure 7(a)) and stage (ii) (Figure 7(b)) is 1086.01 cm^{-1}, and that of stage (iii) (Figure 7(c)) and stage (iv) (Figure 7(d)) is 1085.40 cm^{-1}. That is to say, the minerals of the sparry cements are calcites [31]. Although the contents of Fe^{2+} and Mn^{2+} can affect the properties of calcite cements under cathodoluminescence, the different contents of Fe^{2+} and Mn^{2+} in the calcite cement have little effect on the Raman shift of calcite.

The peaks of the host minerals will not be discussed in the subsequent contents. There are five peaks in the gas inclusion (Figure 8(a)). The Raman shifts of the peaks are 1270.66 cm^{-1}, 1370.89 cm^{-1}, 2322.85 cm^{-1}, 2911.93 cm^{-1}, and 2952.79 cm^{-1}. The corresponding compounds are CO_2 (1270.66 cm^{-1} and 1370.89 cm^{-1}), N_2, CH_4, and C_2H_6, respectively.

There are four peaks in the vapor phase of the two-phase aqueous fluid inclusion (Figure 8(b)). The Raman shifts of the peaks are 1268.87 cm^{-1}, 1371.67 cm^{-1}, 2915.30 cm^{-1}, and 2957.05 cm^{-1}. The corresponding compounds are CO_2 (1268.87 cm^{-1} and 1371.67 cm^{-1}), CH_4, and C_2H_6, respectively.

There are a bump and a peak in the vapor phase of another two-phase aqueous fluid inclusion (Figure 8(c)). The Raman shift of the bump is 1311.24-1640.53 cm^{-1}, which indicates the vapor phase may contain asphaltine (D band of disordered graphite ~1355 cm^{-1}; G band of well-ordered graphite ~1575-1582 cm^{-1}) and light hydrocarbon components such as C_6H_{14} (1451 cm^{-1}) and C_7H_{16} (1302 cm^{-1}) [31]. The Raman shift of the peak is 2912.02 cm^{-1}, which represents CH_4.

There are a bump and three peaks in the liquid phase of the two-phase aqueous fluid inclusion (Figure 8(d)). The Raman shift of the bump is 3200-4000 cm^{-1}, which represents water. The Raman shifts of the three peaks are 1040.74 cm^{-1}, 1063.41 cm^{-1}, and 2916.32 cm^{-1}. The corresponding compounds (ions) are NO_3^-, CO_3^{2-}, and CH_4, respectively.

Through the identification of hydrocarbon gases, it is shown that the two-phase aqueous inclusions which were used in microthermometry were formed in the same period as hydrocarbon inclusions. The two-phase aqueous inclusions in the microthermometry were not syntaxial inclusions which were formed by the trapping of seawater. That is to say, the petrographic analysis results of FIA are verified, and the validity of microthermometry data is also confirmed.

4.4. Simulation of Hydrocarbon Generation and Expulsion History. The hydrocarbon generation and expulsion history of three sets of source rocks in the ADRRB were simulated, so as to provide a basis for the judgment of the hydrocarbon accumulation period. The hydrocarbon generation and expulsion history curves of the three sets of source rocks in ADRRB are shown in Figure 9. The hydrocarbon expulsion time lags behind the hydrocarbon generation time because of the need to satisfy the adsorption by the pores of source rocks. The coal-bearing mudstone began to generate hydrocarbons at 170 Ma and to expel hydrocarbons at about 150 Ma, reaching the hydrocarbon expulsion peak in the Paleogene. The argillaceous limestone and Gap layer began to generate hydrocarbons at 103 Ma and to expel hydrocarbons at around 98 Ma. Compared with the coal-bearing mudstones, the argillaceous limestone and Gap layer have a lower level of hydrocarbon generation and expulsion. Before the Himalayan orogeny, the ADRRB was in a stable subsidence stage, and the rise in the strata temperature promoted the hydrocarbon generation and expulsion in the source rocks. The eastern section of the ADRRB was relatively deep and was the main hydrocarbon kitchen in the ADRRB. With the beginning of the Himalayan orogeny, the eastern section of ADRRB was strongly folded and uplifted, and the most important hydrocarbon kitchen in the ADRRB was destroyed, causing the overall hydrocarbon generation and expulsion in the ADRRB to slow down.

In the geological history period, Murgab depression in the southeast of the basin was located in a relative depression area of the basin; that is, the evolution of the Murgab source rocks was ahead of those in the ADRRB. So in the hydrocarbon expulsion stage of the source rocks in the ADRRB, the oil and gas from Murgab depression had already migrated to the ADRRB to charge the traps.

4.5. Hydrocarbon Charging Stages. The studies summarized above show that there are numerous approaches that can be taken to obtain accumulation periods from microscopic analysis of the hydrocarbon reservoirs. The combination method of comprehensive analysis of reservoir charging stages is as follows: (i) Diagenetic stages are divided by cathodoluminescence; (ii) FIAs are identified according to petrographic characteristics; (iii) The entrapment stages of FIAs are divided by UV epifluorescence and microthermometry; (iv) Because the gas components do not emit fluorescence under ultraviolet illumination, the identification of
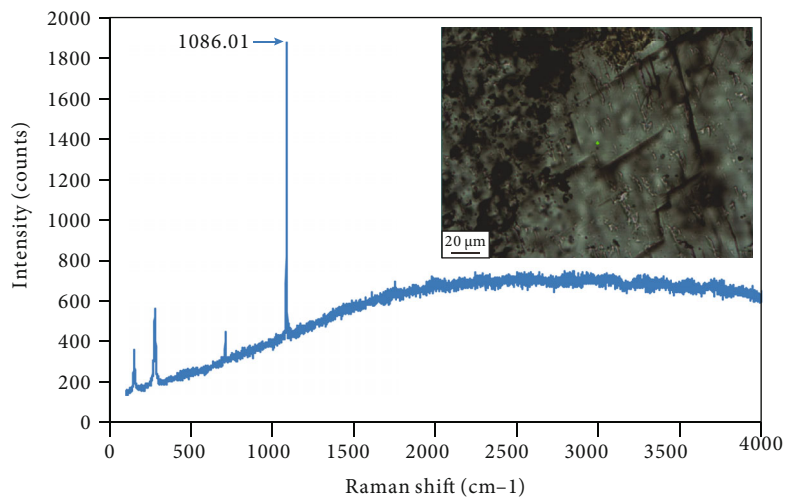
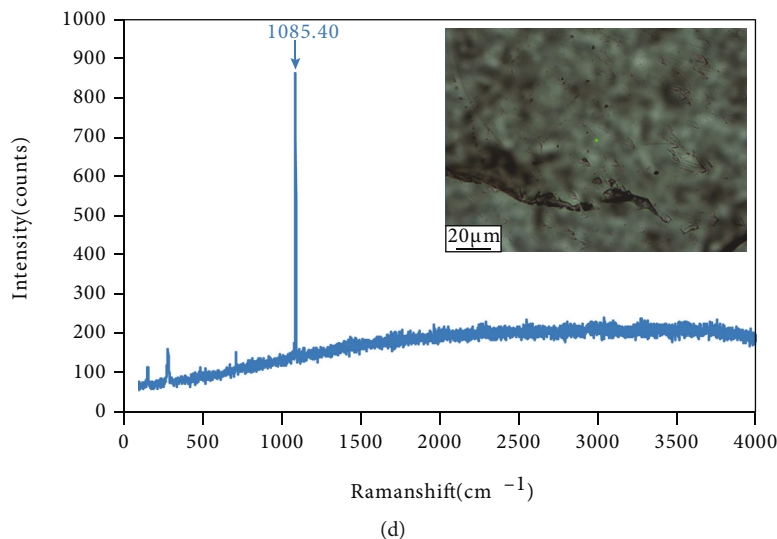(a)
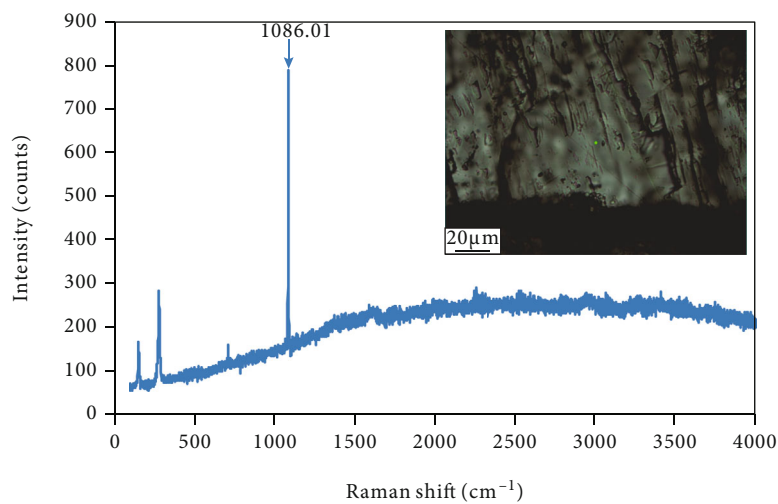
(b)
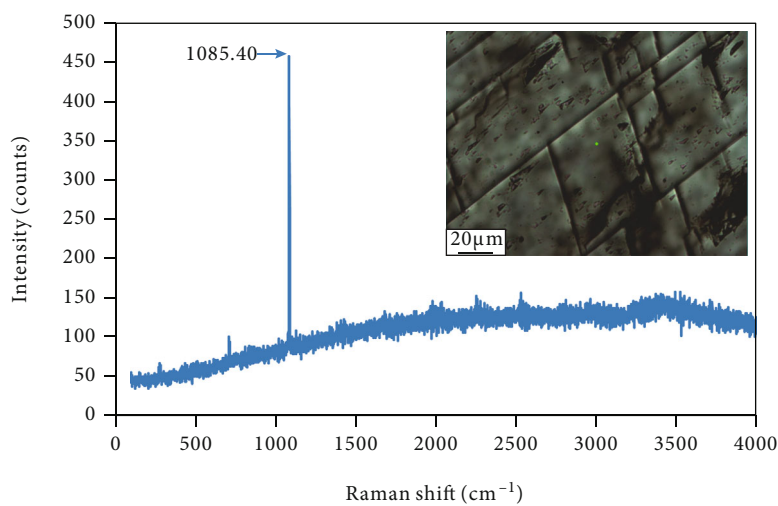
(c)

Figure 7: Continued.

(d)

FIGURE 7: Raman spectra of host minerals in the J_2k-J_3o reservoirs in the ADRRB.

hydrocarbon gas components in gas inclusions by laser Raman can provide evidence for hydrocarbon gas charging. The mineral types of cements can also be determined by laser Raman to verify the conclusions of cement identification by petrographic analysis and cathodoluminescence. Comparisons between fluorescence emission spectra of oil inclusions with API gravity and maturity of related oils show that there is a tendency for petroleum fluorescence to change from yellow to blue colors with increasing maturity [32]. By comprehensively analyzing the occurrence location and fluorescence characteristics of hydrocarbon inclusions, it can be confirmed that:

(i) The yellow fluorescent FIAs were captured in the (Early) Mesogenetic burial stage. During this period, the reservoirs were gradually divorced from the seawater environment and began to capture the fluids in the formation, and the low mature hydrocarbon and formation water were sealed in the crystal

(ii) The green fluorescent FIAs were entrapped in the (Late) Mesogenetic burial stage. Under the increasing formation temperature, the sparry calcite cements continued to crystallize, formed well-developed cleavage fissures, and trapped the maturer oil that had migrated into the reservoirs

(iii) The blue fluorescent FIAs and gas inclusions containing CH_4 were captured during the Telogenetic burial stage. The tectonic movement made the reservoirs produce fractures which are filled with calcite precipitated from the formation water. The highly mature oil and hydrocarbon gas were sealed in the sparry calcite crystal

The timing of hydrocarbon charging can be quantified by projecting the T_h of FIAs onto the burial (thermal) history map [32–34]. According to the microthermometry data

from Well AMO-2 (Figure 6(b)), the homogenization temperature of yellow fluorescent FIAs is 100-110°C, and that of green and blue fluorescent FIAs is 130-140°C. Although green and blue fluorescent FIAs cannot be distinguished by T_h, it can be determined that the entrapment of blue fluorescent inclusions occurred later than that of green fluorescent inclusions by using freezing point depression data, development location, and fluorescence property. The formation of large-scale yellow fluorescent FIAs occurred in 120-105 Ma (Early Cretaceous). At that time, the reservoirs were no longer affected by seawater. Complex physicochemical processes occurred between formation water and reservoirs to precipitate calcite cements from formation water and capture low mature hydrocarbons. The green fluorescent FIAs formed during 75-65 Ma (Late Cretaceous-Early Paleozoic). The rising formation temperature caused the newly precipitated calcite to develop into automorphic crystal with two sets of cleavage fissures. The extension direction of the trapped maturer hydrocarbon FIAs might have cut the cleavage fissures of the calcite. The blue fluorescent FIAs were entrapped in 30-20 Ma (Oligocene-Miocene). The reservoirs experienced the Himalayan tectonic movement, resulting in extensive fractures that provided accommodation for calcite precipitation from formation water. The migrated highly mature oil and hydrocarbon gas inclusions were sealed in calcite veins (Figure 10).

4.6. Restoration of the Hydrocarbon Accumulation Process. Based on the current seismic profile (the section direction is shown in Figure 2(a)) (Figure 11), the structural evolution of the Sandykly uplift in the middle section of the ADRRB is restored by horizon-flattening technique. Combined with diagenetic stages, paleofluid properties, hydrocarbon generation (expulsion) simulation, and the division of oil and gas accumulation stages, the formation process of the hydrocarbon reservoirs in the middle section of the ADRRB can be restored (Figure 12).
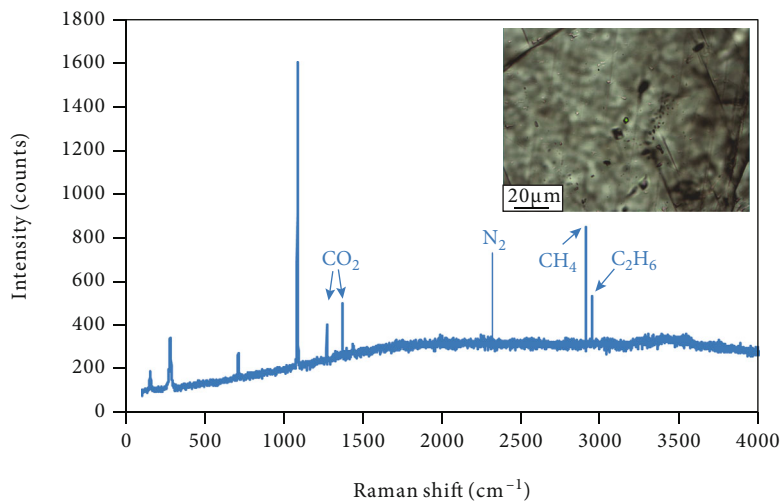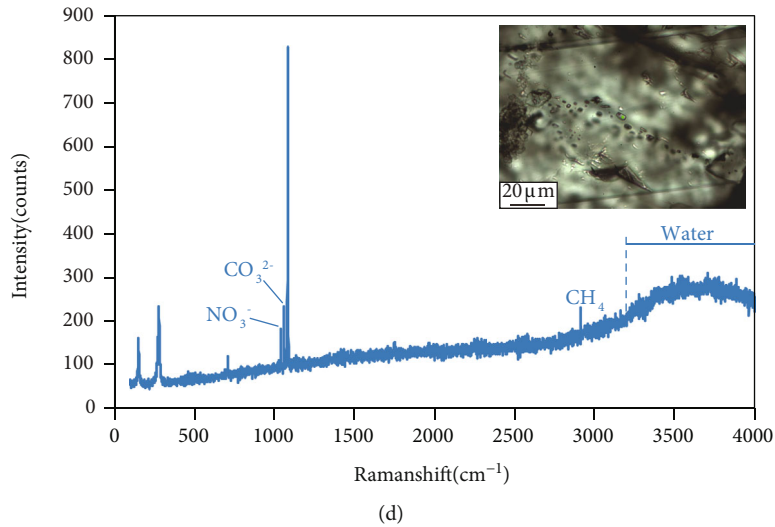
(a)
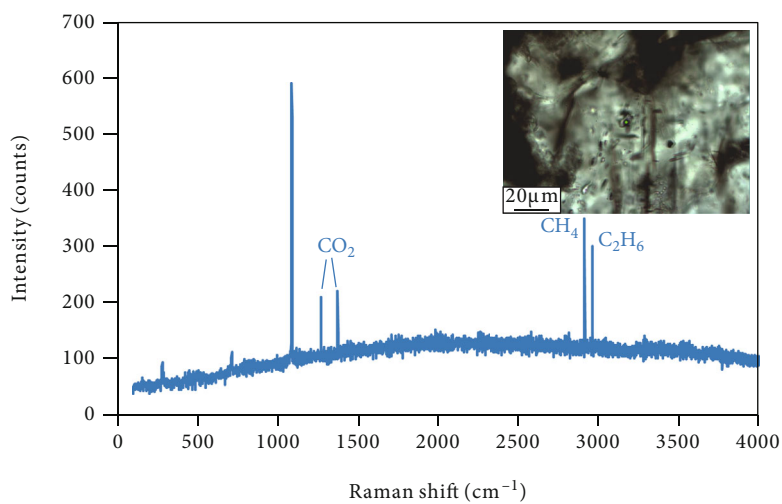
(b)
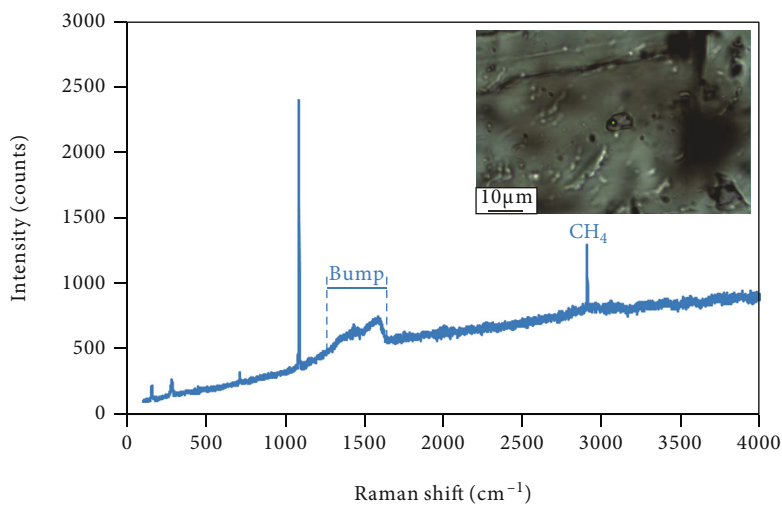
(c)

Figure 8: Continued.

(d)

FIGURE 8: Raman spectra of fluid inclusions in the J_2k-J_3o reservoirs in the ADRRB.
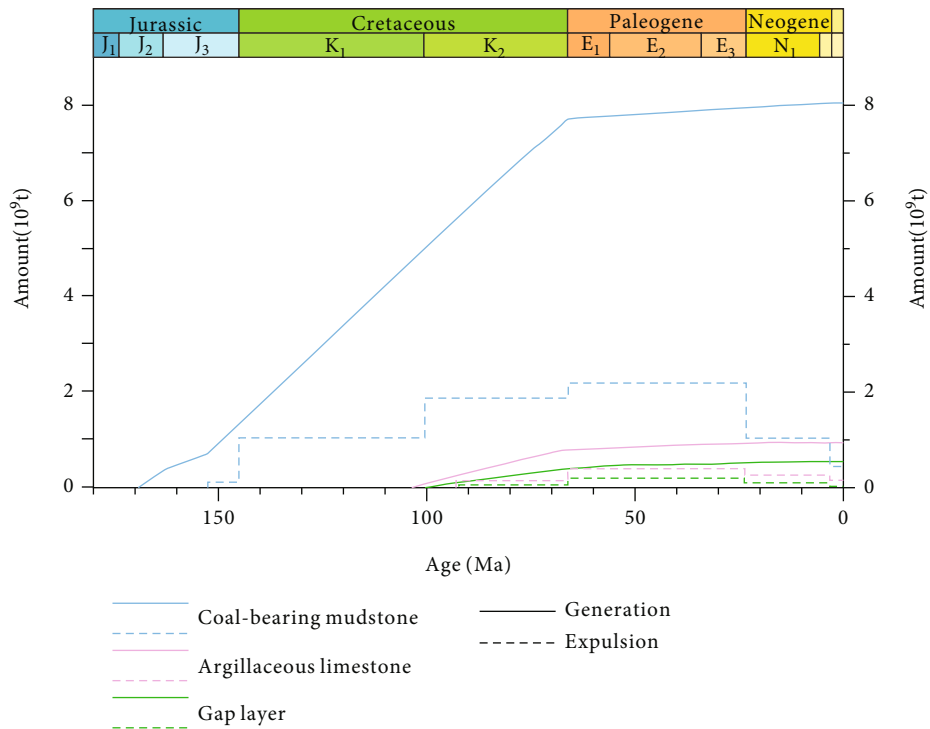

FIGURE 9: Hydrocarbon generation and expulsion curves of the source rocks in the ADRRB.

In the Early Cretaceous, the J_{1-2} coal-bearing mudstones in the Murgab depression in the southeast of the Amu Darya Basin entered the oil generation window and quickly reached the hydrocarbon expulsion peak stage. In the Albian Age (120~105 Ma), the oil and gas generated in the Murgab depression migrated along the unconformity surface between the Jurassic strata and the Paleozoic strata, as well as the basement faults of Chardzhou terrace, to the reef-beach bodies of the southern slope belt of the Sandykly uplift [15, 35]. At this moment, the buried depth of the reservoirs in the middle section of the ADRRB was about 2500 m, and

they entered the (Early) Mesogenetic burial diagenesis stage. Microscopically, the calcites precipitated and crystallized around particles and syntaxial cements, capturing the hydrocarbon that had migrated into the reservoirs and forming the yellow fluorescent FIAs. Macroscopically, the reservoirs were charged with oil and gas to form structural-lithological hydrocarbon reservoirs (Figure 12(a)). Although the hydrocarbon generation and expulsion simulation shows that the coal-bearing mudstones of the ADRRB have reached the first hydrocarbon expulsion peak (Figure 9), the value of the hydrocarbon generation and expulsion curve
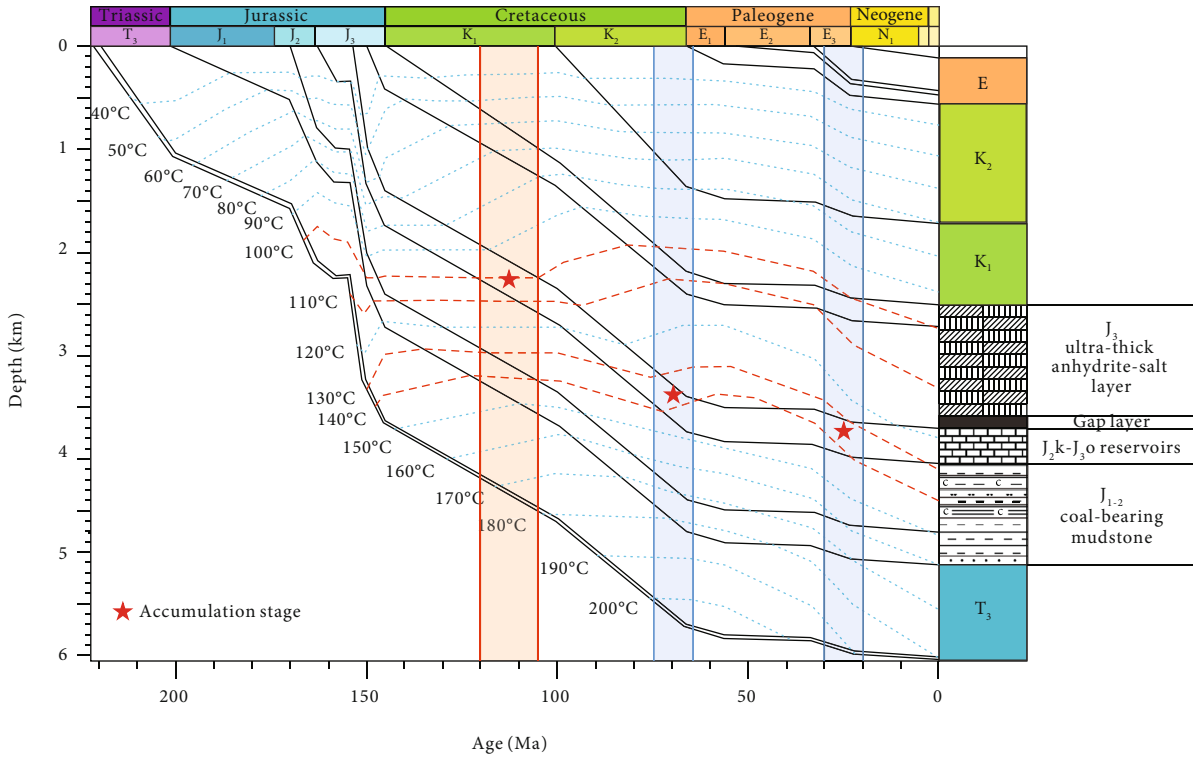
FIGURE 10: Burial-thermal history curves of Well AMO-2 in the middle section of the ADRRB.
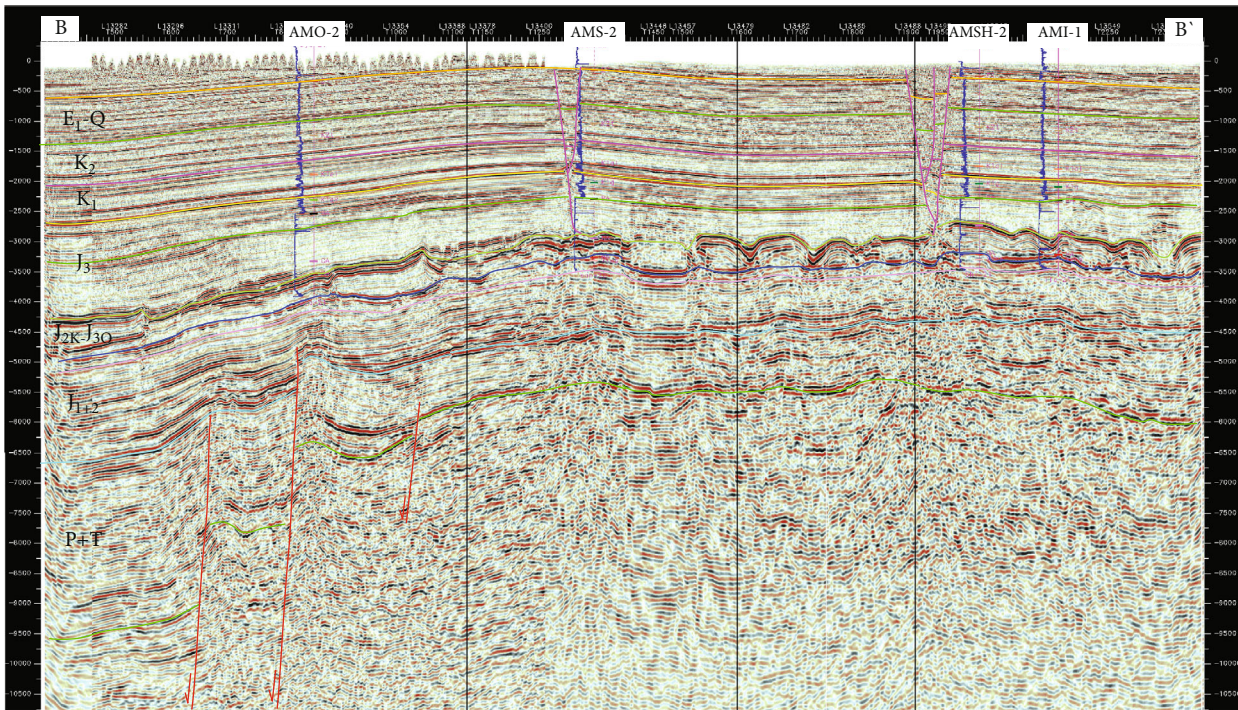

FIGURE 11: Seismic profile of Sandykly uplift in the Amu Darya Right Bank Block.

is mainly contributed by the depression in the east of the ADRRB, which has evolved into the Gissar piedmont thrust belt (Figure 2(a)). The hydrocarbon expelled from the east depression accumulated nearby and had little effect on the middle section of the ADRRB. The buried depth of J_{1-2} coal-bearing mudstones in the middle section of the ADRRB was less than 3000 m (Figure 10); they were in a low-maturity stage with a negligible quantity of hydrocarbon

(a) End of the early Cretaceous sedimentary

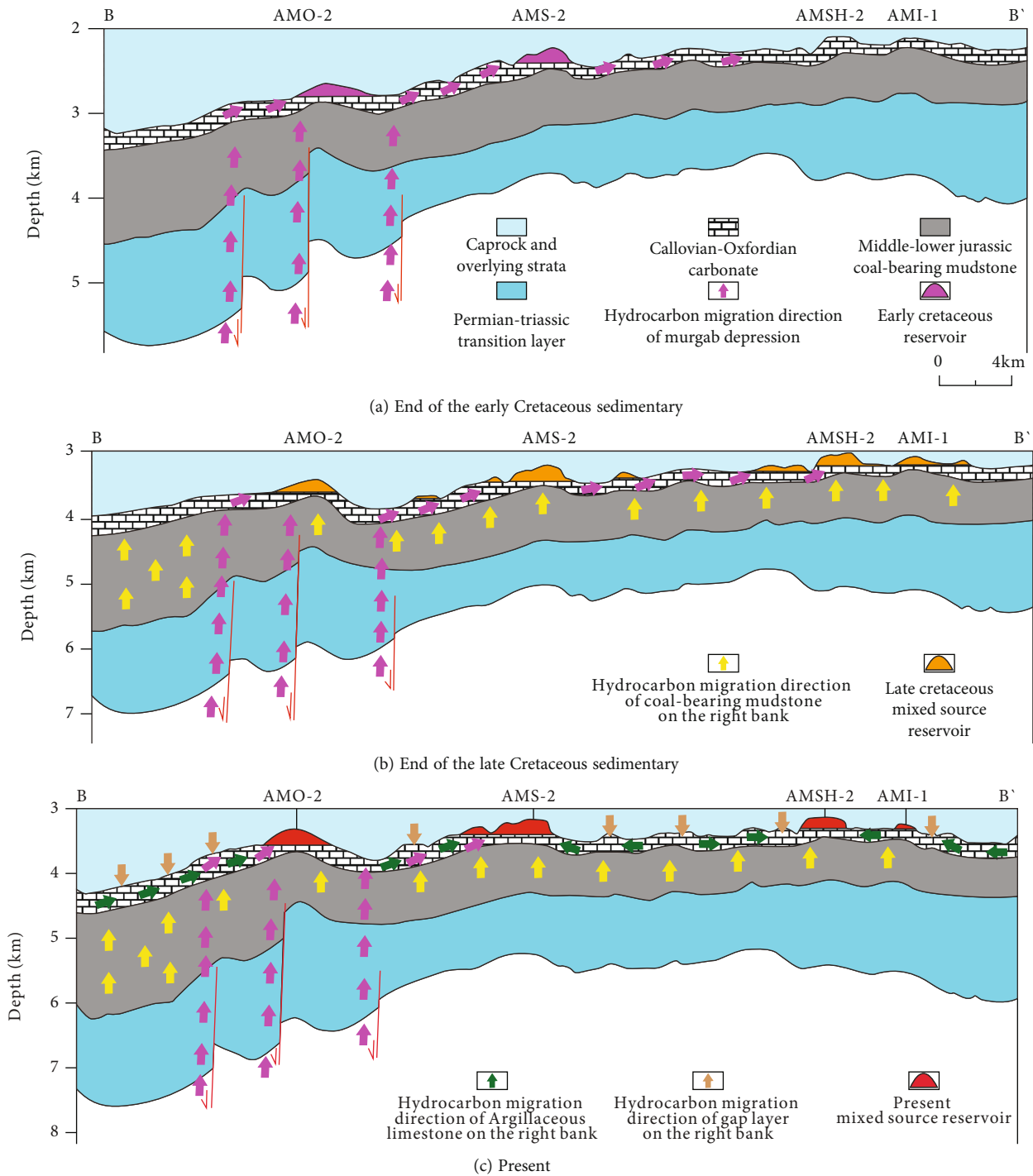(b) End of the late Cretaceous sedimentary

(c) Present

FIGURE 12: Process and model of hydrocarbon accumulation in Sandykly uplift in the Amu Darya Right Bank Block.

generation and expulsion. Therefore, the oil and gas in this period mainly came from the Murgab depression (Figure 12(a)).

During the Turonian Age of the Late Cretaceous (75-65 Ma), the Amu Darya Basin continued to subside. The buried depth of the reservoirs in the middle section of the ADRRB was about 3500 m, and they entered the (Late) Mesogenetic burial diagenesis stage. The massive calcite cements with two sets of cleavage fissures began to capture the hydrocarbon and formation water in the reservoirs to

form green fluorescent FIAs. The source rocks in the Murgab depression expelled vast wet gas. The burial depth of the coal-bearing mudstones in the middle section of the ADRRB exceeded 4000 m, and they began to expel a lot of hydrocarbon. Driven by buoyancy, the hydrocarbon generated by the coal-bearing mudstones in the middle section of the ADRRB migrated upward directly and accumulated in the reservoirs together with the oil and gas that had migrated from the Murgab depression (Figure 12(b)). The argillaceous limestone and Gap layer of the ADRRB

subsequently entered a low-maturity stage in the east section of the ADRRB and expelled a small quantity of hydrocarbons (Figure 9).

From the Paleogene-Oligocene to the Neogene-Miocene (30~20 Ma), the buried depth of the reservoirs in the middle section of the ADRRB was about 4000 m, and they entered the Telogenetic burial diagenesis stage. In terms of reservoir scale, a large number of fractures were produced in the middle section of the ADRRB affected by the compression of the Miocene Himalayan tectonic movement [18]. The newly formed spaces were filled with calcites precipitated from formation water. Blue fluorescent FIAs and hydrocarbon gas inclusions are sealed in these dully luminescent calcite veins. In terms of trap scale, the closure height of the traps in the Sandykly uplift increased slightly. The trap volume was increased in the Sandykly uplift. In terms of basin scale, the coal-bearing mudstones in Murgab depression entered the gas generation window and expelled dry gas; meanwhile, the argillaceous limestone and Gap layer in the middle section of the ADRRB entered the oil generation window. By now, the hydrocarbon reservoirs in the middle section of the ADRRB had been charged by four sources (Figure 12(c)). The source rocks were (i) J_{1-2} coal-bearing mudstones of Murgab depression, (ii) J_{1-2} coal-bearing mudstones of ADRRB, (iii) J_2k-J_3o argillaceous limestone of ADRRB, and (iv) the Gap layer of the ADRRB. Although the hydrocarbon reservoirs are sealed and protected by ultrathick anhydrite-salt layer [16], under strong gas dissipation [36], continuous charging is also essential for the preservation of the hydrocarbon reservoirs of the Amu Darya Right Bank Block. In the follow-up research, it will be necessary to carry out refined oil-source correlation for ADRRB, so as to determine the contribution of each source rock to the hydrocarbon reservoirs and further constrain and optimize the hydrocarbon accumulation model.

5. Conclusion

(1) The J_2k-J_3o carbonate reservoirs in the ADRRB can be divided into four diagenetic stages: (i) Syntaxial stage, (ii) (Early) Mesogenetic burial stage, (iii) (Late) Mesogenetic burial stage, and (iv) Telogenetic burial stage. The cathodoluminescence results show that the cement of J_2k-J_3o reservoirs is calcite. According to the fluorescence characteristics, the hydrocarbon fluid inclusions developed in the sparry calcite cements can be divided into three stages: (I) yellow fluorescent hydrocarbon inclusions in the healing fractures of (ii) stage calcite cement, (II) green fluorescent hydrocarbon inclusions in the healing fractures of (iii) stage calcite cement, and (III) blue fluorescent hydrocarbon inclusions in (iv) stage calcite veins. Laser Raman spectrum shows that the aqueous fluid inclusions coexisting with hydrocarbon inclusions are rich in hydrocarbon gases such as CH_4 and C_2H_6

(2) The ADRRB is in a continuous charging state on the whole. The main peak temperature of T_h histogram

is 100~110°C, representing the overall large-scale hydrocarbon charging stage. In the middle section of the ADRRB, the T_h peak of 100~110°C corresponds to yellow fluorescent hydrocarbon inclusions, and the T_h peak of 130~140°C corresponds to green and blue fluorescent hydrocarbon inclusions. The salinity of the aqueous fluid inclusions coexisting with yellow fluorescent hydrocarbon inclusions is 2.90~8.41%. The salinity of the green fluorescent FIAs is 8.14~12.73% and that of the blue fluorescent FIAs is 4.49~9.86%

(3) In the Albian Age of the Early Cretaceous (120~105 Ma), the reservoirs in the middle section of the ADRRB were charged with oil and gas migrated from the Murgab depression to form structural-lithological hydrocarbon reservoirs. During the Turonian Age of the Late Cretaceous (75-65 Ma), the hydrocarbon generated by the coal-bearing mudstones in the middle section of the ADRRB migrated upward directly and accumulated in the reservoirs together with the oil and gas that had migrated from the Murgab depression. From the Paleogene-Oligocene to the Neogene-Miocene (30~20 Ma), the closure height of the traps in the Sandykly uplift increased affected by the compression of the Miocene Himalayan tectonic movement. The oil and gas generated from J_2k-J_3o argillaceous limestone and the Gap layer of ADRRB began to charge the local reservoirs. Because of the sealing of an ultrathick anhydrite-salt layer and the continuous charging from multiple sources, the hydrocarbon reservoirs formed in the Early Cretaceous can be well preserved up to now

Data Availability

The microthermometry data used to support the findings of this study are included within the article.

Conflicts of Interest

The authors declare that they have no conflicts of interest.

References

[1] H. G. Machel, "Investigations of burial diagenesis in carbonate hydrocarbon reservoir rocks," *Geoscience Canada*, vol. 32, pp. 103–128, 2005.

[2] P. Liu, S. Deng, P. Guan, Y. Jin, K. Wang, and Y. Chen, "The nature, type, and origin of diagenetic fluids and their control on the evolving porosity of the Lower Cambrian Xiaoerbulak Formation dolostone, northwestern Tarim Basin, China," *Petroleum Science*, vol. 17, no. 4, pp. 873–895, 2020.

[3] M. Wang, Y. Chen, W. M. Bain et al., "Direct evidence for fluid overpressure during hydrocarbon generation and expulsion from organic-rich shales," *Geology*, vol. 48, no. 4, pp. 374–378, 2020.

[4] S. Zendehboudi and A. Bahadori, *Shale Oil and Gas Handbook: Theory, Technologies, and Challenges*, Gulf Professional Publishing, 2016.

[5] S. Zendehboudi, I. Chatzis, A. A. Mohsenipour, and A. Elkamel, "Dimensional analysis and scale-up of immiscible two-phase flow displacement in fractured porous media under controlled gravity drainage," *Energy & Fuels.*, vol. 25, no. 4, pp. 1731–1750, 2011.

[6] H. G. Machel, "Bacterial and thermochemical sulfate reduction in diagenetic settings – old and new insights," *Sedimentary Geology*, vol. 140, no. 1-2, pp. 143–175, 2001.

[7] R. H. Goldstein and T. J. Reynolds, "Systematics of fluid inclusions in diagenetic minerals," *Society for Sedimentary Geology Short Course No.*, vol. 31, 1994.

[8] J. Parnell, "Potential of palaeofluid analysis for understanding oil charge history," *Geofluids*, vol. 10, 82 pages, 2011.

[9] I. H. S. Energy, *Field & Reserves dataDB/OL*, 2014, http://www.ihs.com/.

[10] G. Ulmishek, *Petroleum Geology and Resources of the Amu-Darya Basin*, USGS Bulletin 2201-H, Turkmenistan, Uzbekistan, Afghanistan, and Iran, 2004.

[11] R. Zheng, Y. Li, L. Wu, X. Wu, F. Li, and G. Niu, "Geochemical characteristics of Callovian-Oxfordian carbonates in Samandepe gas field, Amu Darya Basin, Turkmenistan," *Turkmenistan. Petroleum Science*, vol. 8, no. 4, pp. 371–381, 2011.

[12] R. Zheng, Y. Pan, C. Zhao, L. Wu, R. Chen, and R. Yang, "Carbon and oxygen isotope stratigraphy of the Oxfordian carbonate rocks in Amu Darya Basin," *Journal of Earth Science*, vol. 1, pp. 42–56, 2013.

[13] J. Dai, B. He, Y. Sun, P. Li, and X. Li, "Formation of the Central-Asia coal-formed gas accumulation domain and its source rocks-series study I on the Central-Asia coal-formed gas accumulation domain," *Petroleum Exploration and Development*, vol. 22, 1996.

[14] C. Wu, B. Yu, H. Wang et al., "High-resolution sequence divisions and stratigraphic models of the Amu Darya right bank," *Arabian Journal of Geosciences*, vol. 12, no. 7, 2019.

[15] F. Li, X. Jing, C. Zou, H. Zhang, and F. Xiang, "Facies analysis of the Callovian-Oxfordian carbonates in the northeastern Amu Darya Basin, southeastern Turkmenistan," *Marine and Petroleum Geology*, vol. 88, pp. 359–380, 2017.

[16] T. Guo, H. Wang, L. Mu et al., "A graphical model for haloanhydrite components and P-wave velocity: a case study of haloanhydrites in Amu Darya Basin," *Applied Geophysics*, vol. 13, no. 3, pp. 459–468, 2016.

[17] Y. Yu, J. Yin, J. Zheng, F. Li, C. Tao, and X. W. H. Xu, "Division and resources evaluation of hydrocarbon plays in the Amu Darya Basin, Central Asia," *Petroleum Exploration and Development*, vol. 42, pp. 750–756, 2015.

[18] A. M. M. Robert, J. Letouzey, M. A. Kavoosi et al., "Structural evolution of the Kopeh Dagh fold-and-thrust belt (NE Iran) and interactions with the South Caspian Sea Basin and Amu Darya Basin," *Marine and Petroleum Geology*, vol. 57, pp. 68–87, 2014.

[19] Y. Cheng, L. Mu, Y. Zhu et al., "Water producing mechanisms of carbonate reservoirs gas wells: a case study of the Right Bank Field of Amu Darya, Turkmenistan," *Petroleum Exploration and Development*, vol. 44, no. 1, pp. 89–96, 2017.

[20] T. Hantschel and A. I. Kauerauf, *Fundamentals of Basin and Petroleum Systems Modeling*, Springer, Berlin/Heidelberg, Germany, 2009.

[21] P. A. Scholle and D. S. Ulmer-Scholle, "A color guide to the petrography of carbonate rocks: grains, textures, porosity, diagenesis," *AAPG Memoir*, vol. 77, pp. 1–486, 2003.

[22] L. D. Stasiuk and L. R. Snowdon, "Fluorescence microspectrometry of synthetic and natural hydrocarbon fluid inclusions: crude oil chemistry, density and application to petroleum migration," *Applied Geochemistry*, vol. 12, no. 3, pp. 229–241, 1997.

[23] I. A. Munz, H. Johansen, K. Holm, and J. Lacharpagne, "The petroleum characteristics and filling history of the Frøy field and the Rind discovery, Norwegian North Sea," *Marine and Petroleum Geology*, vol. 16, no. 7, pp. 633–651, 1999.

[24] I. A. Munz, "Petroleum inclusions in sedimentary basins: systematics, analytical methods and applications," *Lithos*, vol. 55, no. 1-4, pp. 195–212, 2001.

[25] P. J. Eadington, M. Lisk, and F. W. Krieger, *Identifying Oil Well Sites*, United States Patent No.5543616, 1996.

[26] M. Lisk, S. C. George, R. E. Summons, R. A. Quezada, and G. W. O'Brien, "Mapping hydrocarbon charge histories: detailed characterisation of the South Pepper Oil Field, Carnarvon Basin," *Carnarvon basin. APPEA Journal*, vol. 36, no. 1, pp. 445–463, 1996.

[27] R. H. Goldstein, "Petrographic Analysis of Fluid Inclusions," in *Short Course 32*, Mineralogical Association of Canada, 2003.

[28] C. Ramboz, M. Pichavant, and A. Weisbrod, "Fluid immiscibility in natural processes: use and misuse of fluid inclusion data: II. Interpretation of fluid inclusion data in terms of immiscibility," *Chemical Geology*, vol. 37, no. 1-2, pp. 29–48, 1982.

[29] J. J. Wilkinson, "Fluid inclusions in hydrothermal ore deposits," *Lithos*, vol. 55, no. 1-4, pp. 229–272, 2001.

[30] R. J. Bodnar, "Revised equation and table for determining the freezing point depression of H_2O-NaCl solutions," *Geochimica et Cosmochimica Acta*, vol. 57, no. 3, pp. 683-684, 1993.

[31] V. Hurai, M. Huraiová, M. Slobodník, and R. Thomas, *Geofluids: Developments in Microthermometry, Spectroscopy*, Elsevier, Thermodynamics and Stable Isotopes, 2015.

[32] R. K. Mclimans, "The application of fluid inclusions to migration of oil and diagenesis in petroleum reservoirs," *Applied Geochemictry*, vol. 2, no. 5-6, pp. 585–603, 1987.

[33] S. D. Burley, J. Mullis, and A. Matter, "Timing diagenesis in the Tartan Reservoir (UK North Sea): constraints from combined cathodoluminescence microscopy and fluid inclusion studies," *Marine and Petroleum Geology*, vol. 6, no. 2, pp. 98–120, 1989.

[34] J. Zhang, J. Guo, J. Liu, W. Shen, N. Li, and G. Xu, "3D-basin modelling of the Lishui Sag: research of hydrocarbon potential, petroleum generation and migration," *Energies*, vol. 12, no. 4, p. 650, 2019.

[35] Y. He, H. Mu, Y. Kang, Y. Wang, and B. Fan, "Characteristics of an upper Jurassic carbonate ramp in the northern Amu-Darya Basin," *International Journal of Geosciences*, vol. 9, no. 2, pp. 148–159, 2018.

[36] R. G. Miller, "Estimating global oil resources and their duration," *Norwegian Petroleum Society Special Publications*, vol. 6, pp. 43–56, 1996.